

Photogenerated Reactive Oxygen Species and Hyperthermia by Cu₃SnS₄ Nanoflakes for Advanced Photocatalytic and Photothermal Antibacterial Therapy

Yangzi Yang

Shanghai 9th Peoples Hospital Affiliated to Shanghai Jiaotong University School of Medicine

Chengwei Wang

Shanghai 9th Peoples Hospital Affiliated to Shanghai Jiaotong University School of Medicine

Ning Wang

Shanghai 9th Peoples Hospital Affiliated to Shanghai Jiaotong University School of Medicine

Jiixin Li

Shanghai 9th Peoples Hospital Affiliated to Shanghai Jiaotong University School of Medicine

Yingchun Zhu

Chinese Academy of Sciences

Jiantao Zai

Shanghai Jiao Tong University

Jingke Fu

Shanghai 9th Peoples Hospital Affiliated to Shanghai Jiaotong University School of Medicine

Yongqiang Hao (✉ hyq_9hospital@hotmail.com)

Shanghai 9th Peoples Hospital Affiliated to Shanghai Jiaotong University School of Medicine

<https://orcid.org/0000-0003-4454-4221>

Research Article

Keywords: reactive oxygen species, Cu₃SnS₄, photocatalytic, photothermal, antibacterial therapy.

Posted Date: January 31st, 2022

DOI: <https://doi.org/10.21203/rs.3.rs-1291866/v1>

License:   This work is licensed under a Creative Commons Attribution 4.0 International License.

[Read Full License](#)

Version of Record: A version of this preprint was published at Journal of Nanobiotechnology on April 20th, 2022. See the published version at <https://doi.org/10.1186/s12951-022-01403-y>.

Abstract

Background

The rapid spread of infectious bacteria has brought great challenges to public health. It is imperative to explore effective and environment-friendly antibacterial modality to defeat antibiotic-resistant bacteria with high biosafety and broad-spectrum antibacterial property. Results

Herein, biocompatible Cu_3SnS_4 nanoflakes (NFs) were prepared by a facile and low-cost fabrication procedure. These Cu_3SnS_4 NFs could be activated by visible light, leading to visible light-mediated photocatalytic generation of a myriad of reactive oxygen species (ROS). Besides, the plasmonic Cu_3SnS_4 NFs exhibit strong near infrared (NIR) absorption and a high photothermal conversion efficiency of 55.7%. The ROS mediated cellular oxidative damage and the NIR mediated photothermal disruption of bacterial membranes collaboratively contributed to the advanced antibacterial therapy, which has been validated by the efficient eradication of both Gram-negative *Escherichia coli* and Gram-positive methicillin-resistant *Staphylococcus aureus* strains *in vitro* and *in vivo*. Meanwhile, the exogenous copper ions metabolism from the Cu_3SnS_4 NFs facilitated the endothelial cell angiogenesis and collagen deposition, thus expediting the wound healing. Importantly, the inherent localized surface plasmon resonance effect of Cu_3SnS_4 NFs empowered them as an active substrate for surface-enhanced Raman scattering (SERS) imaging and SERS-labeled bacteria detection.

Conclusions

The low cost and biocompatibility together with the solar-driven broad-spectrum photocatalytic/photothermal antibacterial property of Cu_3SnS_4 NFs make them a candidate for sensitive bacteria detection and effective antibacterial treatment.

Background

The continuous and rapid spread of infectious bacteria has brought great challenges to public health. This challenge has been further exacerbated by the excessive use of antibiotics, which cultivates multidrug-resistant “super-bacteria” that may go out of the control of traditional antibiotics treatment^[1]. During the past few years, a series of antibacterial materials, such as peptides, polymers, quaternary ammonium salts, metal oxides, and inorganic nanoparticles^[2–6], have proven as bactericidal or bacteriostatic agents due to their unique antibacterial mechanisms. Although the great potential of the abovementioned antibacterial materials as alternative antibiotics, further clinical applications are limited by their potential biotoxicity and low antibacterial efficiency. It is imperative to explore more effective and environment-friendly antibacterial modality to defeat antibiotic-resistant bacteria with high biosafety and broad-spectrum antibacterial property.

Recently, photocatalytic technology has emerged as a promising option for administrating antibiotic-resistant bacteria in water disinfection^[7, 8]. Photocatalysis involves the use of solar light for activating photocatalysts to split water, followed by the generation of a myriad of reactive oxygen species (ROS) such as hydrogen peroxide (H₂O₂), hydroxyl radicals (•OH), superoxide radicals (O₂^{•-}) and singlet oxygen (¹O₂)^[9-11]. These ROS could react with proteins, lipids, polysaccharides as well as other constituents of bacteria, leading to oxidative damage of bacterial membrane and ultimate cell death^[11-14]. It is noteworthy that ROS-based photocatalysis has been revealed to play a vital role in preventing bacterial biofilms formation, showing great potential for even antibiotic-resistant bacteria^[15]. The ideal properties for photocatalysts in antibacterial therapy are i) facile and low-cost fabrication procedure for future mass application; ii) environment-friendly and high biosafety to normal tissues; iii) efficient photocatalytic reactivity with extended absorption region to achieve full spectrum solar-driven photocatalysis; iv) broad-spectrum antibacterial property for even multidrug-resistant bacteria. Ternary Cu₃SnS₄ is a p-type semiconductor with a high absorption coefficient (~10⁵ cm⁻¹) and a tunable optical band gap (0.8-1.7 eV)^[16]. The narrow band gap of Cu₃SnS₄ enables it an extended absorption in visible and near infrared (NIR) regions. Since semiconductor photocatalysts such as ZnO, TiO₂ and Ag-C₃N₄ composite^[17] commonly are only active in the ultraviolet (UV) light spectrum, which occupies only 4% of the solar spectrum^[7]. The higher and extended optional absorption of Cu₃SnS₄ in the visible region (occupies 44% of the solar spectrum) thus makes it a desired photocatalyst for visible (Vis) light activatable antibacterial applications. More importantly, the plasmonic Cu₃SnS₄ exhibits strong NIR absorption and high quantum efficiency, which could be converted to thermal energy and induce NIR based photothermal sterilization^[18-20]. Notably, unlike the narrow bandgap metal sulfides such as CdS, PbS, ZnInS₄, AgGaS₂ and ZnCdS, which suffer from drawbacks of elemental toxicity (Cd and Pb) and higher costs (In and Ga). The Cu₃SnS₄ is consisted of low-cost and non-toxic elements of Cu, Sn and S, which have been reported to play a vital role in regulating the metabolic activity in skin pigmentation, tissue repairs, and acting as building blocks of proteins and tissues^[21, 22].

Herein, we presented a facile and low-cost fabrication procedure for Cu₃SnS₄ nanoflakes (NFs) and proposed a Vis-mediated photocatalytic and NIR-activated photothermal synergistic therapeutic strategy for combating the infections of both Gram-negative *Escherichia coli* (*E. coli*) and Gram-positive methicillin-resistant *Staphylococcus aureus* (MRSA) strains. The underlying antibacterial mechanism was carefully investigated and it was proposed that the ROS mediated cellular oxidative damage and NIR mediated photothermal disruption of bacterial membranes as well as physical contact collaboratively led to the advanced antibacterial therapy. A mouse skin defect and epidermal infected model were established *in vivo*, showing effective bacteria eradication and favorable healing effects with negligible biotoxicity. Moreover, the inherent localized surface plasmon resonance (LSPR) effect of Cu₃SnS₄ NFs empowered them as an active substrate for surface-enhanced Raman scattering (SERS) imaging and SERS-labeled bacteria detection. Overall, the low cost and biocompatibility together with the solar-driven broad-spectrum photocatalytic/photothermal antibacterial property of Cu₃SnS₄ NFs make them a

candidate for sensitive bacteria detection and effective antibacterial treatment, showing great potential for future clinic applications.

Results And Discussion

Construction and characterization of Cu_3SnS_4 NFs

Cu_3SnS_4 NFs were fabricated *via* a modified solvothermal procedure^[23, 24]. As shown in the transmission electron microscopy (TEM) images in **Figure 1A**, nearly monodispersed foliate Cu_3SnS_4 NFs were produced. Notably, these NFs were built up by nanocrystals, as can be seen from the high-resolution TEM images and the selected area electron diffraction (SAED) pattern (Figure 1B, Figure S1 and S2). The element mappings in Figure 1C indicate that each element of Cu, Sn and S was presented and distributed in the framework of Cu_3SnS_4 NFs uniformly. The energy-disperse X-ray spectrum (EDS) shows the distribution of Cu, Sn and S elements without the presence of any other impurities (Figure 1D). The atomic ratio of Cu:Sn:S is about 2.4:1:3.26, indicating Cu and S vacancies compared with the stoichiometric ratio of Cu_3SnS_4 . The crystal structure of as-prepared Cu_3SnS_4 NFs was further characterized by X-ray diffraction (XRD). As shown in Figure 1E, the diffraction peaks at 2θ values of 28.5, 47.5, and 56.0 were assigned to the (112), (220) and (132) crystal planes of tetragonal Cu_3SnS_4 (JCPDS card No. 33-0501). No impurities can be found in the XRD pattern, indicating the pure phase of Cu_3SnS_4 without secondary phases. The zeta potential analysis shows that the surface of Cu_3SnS_4 NFs was positively charged (+6.3 mV) in deionized water (Figure 1F). X-ray photoelectron spectroscopy (XPS) was used to further explore the oxidation state of Cu, Sn and S elements in the Cu_3SnS_4 . The XPS survey spectrum reveals the presence of Cu, Sn and S peaks (Figure S3). The binding energies of the $\text{Cu}2p_{3/2}$ and $\text{Cu}2p_{1/2}$ centered at 932.1 eV and 952.1 eV respectively (Figure 1G1), which could be typically assigned to Cu^+ species^[25]. Additionally, the $\text{Cu}2p_{3/2}$ satellite peak at 942.8 eV could be identified as Cu^{2+} species^[25], suggesting the presence of both Cu^+ and Cu^{2+} species in the Cu_3SnS_4 NFs. The binding energies of the $\text{Sn}3d_{5/2}$ and $\text{Sn}3d_{3/2}$ centered at 486.8 eV and 495.2 eV respectively (Figure 1G2), corresponding to the reported values for Sn^{4+} ^[26]. No evidence of Sn^{2+} (binding energy at 485.2 eV) was detected in the sample. The S2p core-level spectrum indicated the binding energy at 161.9 eV (Figure 1G3). Additional peak at 168.9 eV was also detected, which may be attributed to the oxidized parts of the product.

The photocatalysis mediated ROS generation from Cu_3SnS_4 NFs

As shown in **Figure 2A**, the typical optical absorption range of Cu_3SnS_4 NFs crosses from the UV to NIR region (250-1000 nm), highly desirable for full spectrum solar-driven photocatalysis and photothermal antibacterial treatment. The visible light mediated photocatalytic ROS generation was initially evaluated

by methylene blue (MB) degradation kinetics, which was monitored by an UV/Vis spectrophotometer. Under visible light irradiation, time-dependent decolorization of MB was observed after incubation with Cu_3SnS_4 NFs for different times (Figure 2B). The degradation of MB was confirmed by its characteristic absorbance at 664 nm, which decreased with the reaction proceeding (Figure 2C). Since both Cu^+ and Cu^{2+} are presented in the Cu_3SnS_4 NFs, it was expected that the Cu ions mediated Fenton-like reaction may boost the ROS generation and further exacerbate the degradation of MB^[27]. As observed, the adding of tiny H_2O_2 (1 mM) into the reaction mixture greatly improved the time-dependent degradation efficiency (Figure 2D, E). It was noted that almost no degradation of MB occurred in 1 mM H_2O_2 solution without the Cu_3SnS_4 catalyst, demonstrating the photocatalysis mediated generation of ROS and degradation of MB. In advanced oxidation technologies, hydroxyl radicals ($\cdot\text{OH}$) are known as one of the key active species for MB degradation with a redox potential of +2.8 V (versus NHE) in acidic media and +1.5 V (versus NHE) in basic media^[28]. To test whether $\cdot\text{OH}$ was generated during the Cu_3SnS_4 mediated photocatalytic process, *t*-butanol (*t*-BuOH), a powerful $\cdot\text{OH}$ scavenger^[29], was pre-added to the reaction mixture to investigate whether the degradation could be retarded. It was found that the adding of *t*-BuOH resulted in a concentration-dependent decrease of the MB degradation but not completely quench the reaction (Figure 2F and Figure S4). It is reasonable to speculate that other radical species may be involved in the MB degradation. Here, sodium azide (NaN_3 , 5 mM), a well-known scavenger for the singlet oxygen ($^1\text{O}_2$)^[30, 31], was pre-added to the reaction mixture. As expected, the MB degradation was significantly restrained in the presence of NaN_3 , suggesting the involvement of $^1\text{O}_2$ in the Cu_3SnS_4 mediated MB degradation (Figure 2F). Similarly, the adding of benzoquinone (1 mM), a scavenger of the superoxide radical ($\text{O}_2^{\cdot-}$)^[32], also greatly alleviated the MB degradation, indicating the occurrence of $\text{O}_2^{\cdot-}$ in the degradation. These data revealed that $\cdot\text{OH}$, $^1\text{O}_2$, and $\text{O}_2^{\cdot-}$ possibly occurred and participated in the MB degradation process. In addition, to directly prove the Cu_3SnS_4 mediated ROS generation, the content of $\cdot\text{OH}$, $^1\text{O}_2$, and $\text{O}_2^{\cdot-}$ was detected by electron paramagnetic resonance (EPR) using DMPO (5,5-dimethyl-1-pyrroline *N*-oxide) and TEMPO (2,2,6,6-tetramethylpiperidine-1-oxyl) as spin probes^[33]. As demonstrated in Figure 2G-I, the main active species including $\cdot\text{OH}$, $^1\text{O}_2$, and $\text{O}_2^{\cdot-}$ could be produced by the Cu_3SnS_4 NFs under visible light irradiation. Importantly, the amount of $\cdot\text{OH}$, $^1\text{O}_2$, and $\text{O}_2^{\cdot-}$ all gradually increased with the prolonged irradiation time. These ROS may further attack bacteria around the photocatalyst and contribute to efficient antibacterial treatment.

The NIR mediated hyperthermia of Cu_3SnS_4 NFs

Cu_3SnS_4 possesses obvious localized surface plasmon resonances (LSPR) in the NIR band^[23, 34]. It was speculated that the strong NIR absorption of Cu_3SnS_4 NFs observed in this work could be attributed to LSPR, which may further lead to photothermal effect for antibacterial treatment. Here, different concentrations of Cu_3SnS_4 NFs were dispersed in aqueous solutions and exposed to an 808 nm NIR laser irradiation for different times. **Figure 3A-C** clearly displays the concentration and irradiation time-

dependent photothermal conversion of Cu_3SnS_4 NFs. The solution temperature was precisely controlled between 25 °C and 52 °C by varying the Cu_3SnS_4 concentration or the irradiation time of the NIR light. In contrast, the temperature change of pure water was less than 2 °C under otherwise identical experimental conditions. Importantly, the photothermal conversion of Cu_3SnS_4 NFs was also found to be laser power density-dependent, showing distinct temperature increase when promoting the laser power density from 0 W cm^{-2} to 2.5 W cm^{-2} (Figure 3D, E). Nine successive cycles of heating/cooling processes demonstrated the stable photothermal conversion capability, which is of key importance for photothermal agents during photothermal treatment (Figure 3F). The photothermal conversion efficiency of Cu_3SnS_4 NFs was calculated to be 55.7% (Figure 3G, H). The Cu ions released from the Cu_3SnS_4 NFs were evaluated by inductively coupled plasma optical emission spectrometry (ICP-OES). 5.1% of Cu ions was released from the Cu_3SnS_4 NFs within 24 h and 5.8% within 48 h in PBS (pH 7.4), respectively (Figure 3I). Besides, it was found that the NIR irradiation (808 nm, 2 W cm^{-2} , 10 min) did not show distinct interference on the release of Cu ions.

***In vitro* antibacterial activity**

Considering the excellent properties of Cu_3SnS_4 NFs as described above, we set out to examine the possibility of the NFs as a potential photocatalytic agent in combination with the photothermal performance for synergistic elimination of bacteria. Here, the synergistic antibacterial activities of Cu_3SnS_4 NFs against both Gram-negative and Gram-positive bacteria were evaluated using *E. coli* and MRSA as model strains, respectively. The relative bacterial cells survival was calculated and the colony forming unit (CFU) plate counting method was used to assess the photo-activated disinfection ability of Cu_3SnS_4 NFs (Figure S5). As shown in **Figure 4A** and Figure S6, both bacteria of *E. coli* and MRSA did not show apparent response to only visible light treatment in the absence of the Cu_3SnS_4 NFs and the cell survival was accordingly used as the control group (Group I). In contrast, the bacterial cells survival dramatically decreased to 46.8% (*E. coli*) and 24.1% (MRSA) after treating with Cu_3SnS_4 at the concentration of 50 $\mu\text{g mL}^{-1}$ under visible light for 20 min (Group III), demonstrating the Cu_3SnS_4 NFs mediated inactivation of both bacteria strains. Notably, the bacterial cells survival further decreased to 22.8% (*E. coli*) and 16.5% (MRSA) after the Cu_3SnS_4 plus 808 nm NIR treatment (10 min) under otherwise identical conditions (Group IV). Since NIR alone (Group II, 808 nm, 1.5 W cm^{-2} , 10 min) did not show any antibacterial effect against both strains (Figure S7), the enhanced antibacterial effect after the Cu_3SnS_4 plus NIR treatment thus could be attributed to the NIR activated and synergistic photothermal effect of Cu_3SnS_4 . Moreover, the photo-activated disinfection activity of Cu_3SnS_4 NFs could be further enhanced by increasing the dose of the NFs (Figure 4A). The bacterial cells survival further decreased to 36.4% for *E. coli* and 19.6% for MRSA when promoting the Cu_3SnS_4 NFs dose to 100 $\mu\text{g mL}^{-1}$. The CFU plate counting provides a more intuitive characterization of the disinfection ability of Cu_3SnS_4 NFs (Figure 4B, C). The antibacterial results under only NIR laser irradiation (group II) was almost the same as that in the control group (group I). In contrast, with the Cu_3SnS_4 NFs treatment, a drastic decrease of MRSA colonies

was observed and even no *E. coli* colonies could be detected under only visible light irradiation for 20 min (group III). More significant disinfection efficiency and complete inhibition of bacterial growth were detected in both bacterial models after the Cu_3SnS_4 NFs plus NIR treatment (group IV), demonstrating the remarkable antibacterial ability of photo-activated Cu_3SnS_4 NFs (Figure 4B, C). The tiny Cu ions released from the Cu_3SnS_4 NFs were found to play a negligible role on the antibacterial activity of the NFs, as verified by the extract liquid results (Figure S8). Fluorescence staining of live/dead cells was performed to further verify the feasibility of eliminating bacteria with different treatments. As shown in the confocal laser scanning microscopy (CLSM) images in Figure 4D, compared with the green fluorescence displayed in both the control group (group I) and the NIR group (group II), a number of dead cells (red fluorescence) were clearly detected in both strains after incubation with Cu_3SnS_4 NFs even without laser irradiation (group III), which was consistent with the bacterial cell survival results. As expected, treatment with Cu_3SnS_4 NFs plus NIR irradiation induced almost complete death of both bacterial cells, indicating their synergistic and stronger cell-killing effect (group IV).

In this study, we rationalized the efficient antimicrobial activity of Cu_3SnS_4 NFs on the basis of the photocatalysis-mediated ROS generation, which further induced the oxidative stress to kill bacterial cells. To highlight this property, the ROS level in MRSA bacterial cells were explored by 2',7'-dichlorodihydrofluorescein diacetate (DCFH-DA) staining, which acts as a commonly used method to evaluate the overall oxidative stress level in cells. As exhibited in **Figure 5A** and Figure S9, bacteria treated with Cu_3SnS_4 NFs with or without NIR irradiation displayed an elevated level of intracellular ROS, which may contribute to the observed antibacterial efficacy of Cu_3SnS_4 NFs. Since both Cu^+ and Cu^{2+} are presented in the Cu_3SnS_4 NFs, it was expected that the Cu ions mediated Fenton-like reaction together with the visible light mediated photocatalysis may collaboratively result in the ROS overproduction (Figure 5B). To further investigate the antibacterial mechanism of photo-activated Cu_3SnS_4 NFs, the cell morphologies of both *E. coli* and MRSA following different treatments were studied by scanning electron microscopy (SEM, Figure 5C). Indeed, in contrast to the well-maintained cell morphology in the control group (group I) and NIR group (group II), distorted cell morphology with lesions and holes on the bacterial cell wall/membranes were observed in both bacterial strains after treatment with Cu_3SnS_4 NFs with or without NIR irradiation (group III and group IV). The photogenerated ROS and hyperthermia were presumed to contribute to the cell membrane damage jointly. Besides, a mass of NFs were discovered on the surface of bacteria. Since the surface of bacteria are commonly negatively charged due to the presence of teichoic acids in the cell wall of Gram-positive bacteria and lipopolysaccharide in the outer membrane of Gram-negative bacteria^[15], it could be speculated that the electrostatic interaction between the positively charged NFs and the negatively charged bacteria would facilitate the preferential absorption (physical contact) of NFs and reinforce the photocatalysis-based antibacterial efficacy by compromising bacterial membrane integrity^[35] (Figure 5D).

***In Vivo* Antibacterial Activity**

The *in vitro* biocompatibility of as-prepared Cu_3SnS_4 NFs was evaluated prior to their *in vivo* biomedical applications. The cytotoxicity of Cu_3SnS_4 NFs to human umbilical vein endothelial cells (HUVEC) and mouse skin fibroblast L929 cells were evaluated, showing no significant toxicity in the wide concentration range of 10-100 $\mu\text{g mL}^{-1}$ within 24 h and 48 h (Figure S10). To assess the *in vivo* antibacterial efficacy of Cu_3SnS_4 NFs, ICR mice with a MRSA-infected cutaneous wound model were fabricated. Initially, the *in vivo* photothermal effect was explored and shown in **Figure 6A**. In contrast to the control group, which showed no distinct change of temperature in the wound area of mice (33.8 °C after 10 min of laser treatment), significantly increased temperature was found in the wound area of the mice treated with Cu_3SnS_4 NFs under the NIR laser irradiation. To be noted, the temperature in the wound area was irradiation time-dependent, which could rapidly reach 49.2 °C in 2 min and maintain around 50 °C in the following 8 min (Figure 6B). Despite the hyperthermia, no obvious normal tissue damage was observed due to the specific and focused laser irradiation toward the wound area. Then, the photo-activated skin wound-healing ability of Cu_3SnS_4 NFs in wound-infecting mice was evaluated. The treatment process is shown in Figure 6C. A rounded cutaneous wound model (6 mm in diameter) was constructed in male ICR mice. Then, MRSA, a common cause of skin infections, was used to construct the wound infecting model. Afterwards, the MRSA-infected mice were divided into four groups (n = 6 for each group) and treated with i) PBS (control group), ii) PBS followed by 808 nm NIR laser irradiation (NIR group), iii) Cu_3SnS_4 dispersed in PBS (Cu_3SnS_4 group), iv) Cu_3SnS_4 dispersed in PBS followed by 808 nm NIR laser irradiation (Cu_3SnS_4 + NIR group), respectively. Mice in all groups were exposed to visible light during the treatment. The size of the wound and weight of each mouse were recorded every two days. As shown in Figure 6D, mice treated with PBS or NIR alone did not show distinct healing of wound despite the presence of scars in both groups (control and NIR group). Significantly, the wound area of mice treated with Cu_3SnS_4 (Cu_3SnS_4 group) was generally smaller, showing around 93.5% recovery on day 8 (Figure 6E). More importantly, mice treated with Cu_3SnS_4 plus NIR irradiation (Cu_3SnS_4 + NIR group) displayed more pronounced recovery of wound. The trauma area on day 4 has exhibited significant difference as compared to the Cu_3SnS_4 group ($^*p < 0.05$, Figure 6E), demonstrating the promoted antibacterial and wound healing efficiency based on the collaborative photocatalytic and photothermal antibacterial effects. To further investigate the wound healing process, the wound skin in each group was harvested and exposed to Hematoxylin and eosin (H&E) staining after the treatment. As shown in Figure 6F, the wound boundary between the wound and normal tissue could be observed clearly from the histological staining results. The keratinocytes migrated to the wound area from the normal tissue and scars became significantly smaller and even vanished after the treatment with Cu_3SnS_4 NFs or Cu_3SnS_4 NFs plus NIR irradiation, whereas incomplete dermal layer was still observed in the control and NIR groups. Besides, the histological slices of both the control group and NIR group presented a number of inflammatory cells, predominantly neutrophils and mononuclear cells adhered to the stratified squamous epithelium. In contrast, intact epidermal layer accompanied with dramatic decrease of the infiltration of inflammatory cells was found after the treatment with Cu_3SnS_4 or Cu_3SnS_4 plus NIR irradiation, further indicating the efficiency of the photo-activated antibacterial effect of the Cu_3SnS_4 NFs.

In vivo evaluation of collagen deposition and angiogenesis in wounds

Wound healing is a dynamic process that involves the proliferation of fibroblasts, deposition of collagen fibers, angiogenesis, formation of granulation tissue, scar formation, wound contraction and epithelialization^[36]. The synthesis and deposition of collagen is a critical factor in wound healing. Cu ions have been recognized as a cofactor to lysyl oxidase, which stimulates the expression of matrix metalloproteinase-2 and collagen in fibroblasts, facilitating wound healing^[37-39]. Histological analysis of Masson's trichrome stained sections showed extensive collagen deposition and a smaller granulation tissue gap in the wounds after the treatment with Cu₃SnS₄ (**Figure 7A, B**). Importantly, more wavy collagen fibers were observed in the wounds of the Cu₃SnS₄ + NIR group, demonstrating the favourable extracellular matrix remodeling of granulation tissue and regeneration of the epidermis^[40]. Further, immunofluorescence staining for CD31, a transmembrane protein expressed early in vascular development, was used to evaluate the newly formed vessels^[41]. It showed that the density of newly formed vessels in the wounds of the Cu₃SnS₄ and Cu₃SnS₄ + NIR group was more significant compared with the other two groups (Figure 7C). The Western blot analysis of CD31 was in concordance with the immunofluorescence staining results, further confirming the promoted vessel number after the treatments (Figure 7D). Moreover, it has been suggested that hypoxia plays a critical role in cell recruitment, cell differentiation and blood vessel formation^[42]. Hypoxia inducible factor-1 α (HIF-1 α) has been identified to initiate the transcription of hypoxia sensitive genes including vascular endothelial growth factor (VEGF) under hypoxic conditions^[43]. Stabilization and activation of HIF-1 α expression was thus suggested as a potential strategy to promote neovascularization^[44]. The HIF-1 α expression and VEGF secretion in wounds after the treatment were then investigated, trying to figure out the angiogenesis during the wound healing process. The HIF-1 α expression, as determined by the Western blot analysis, was promoted both in the Cu₃SnS₄ and Cu₃SnS₄ + NIR group as compared with the other two groups (Figure 7D, E). Moreover, the immunofluorescence staining of VEGF showed more significant expression of VEGF and therefore more new blood vessel formation after the Cu₃SnS₄ and Cu₃SnS₄ + NIR treatment (Figure 7C). The promotion of angiogenesis was expected to allow more supply of oxygen and nutrients as well as accelerated migration of requisite cells and humoral factors into wounds, which leads subsequently to the increased formation of granulation tissue, collagen synthesis and eventually improved wound healing^[38].

Furthermore, the *in vivo* biosafety after the Cu₃SnS₄ and/or NIR treatment was evaluated. The body weight of mice in each group during the whole treatment process did not show distinct difference (Figure S11). Besides, the main blood biochemistry and hematology analyses of mice in each group after the treatment were conducted, suggesting normal functions in liver and kidney (Figure S12). The routine blood test was further assessed to monitor the systemic inflammatory activity, showing no significant differences as compared with the control group (Figure S13). Moreover, no visible damage, inflammation, or abnormality were observed in the histological evaluation of major organs including heart, liver, spleen,

lung, and kidney (Figure 7F). Collectively, the biosafety analyses substantiate that the photo-activated antibacterial treatment showed no obvious side-effect to mice *in vivo*.

Cu₃SnS₄ NFs as an active SERS substrate for the detection of *E. coli* *in vitro*

Surface-enhanced Raman scattering (SERS) imaging is a highly sensitive tool that allows direct identification of target analytes in proximity to the surface of plasmonic nanoparticles^[45]. Due to its high sensitivity, chemical specific, high resolution, and non-destructive characteristics, SERS imaging has demonstrated applications in biomedicine as a promising tool for real-time bacteria detection^[46]. Cu₃SnS₄ compound is a p-type semiconductor due to the presence of copper vacancies, which further endows Cu₃SnS₄ with localized surface plasmon resonance (LSPR) in the NIR region^[47]. Indeed, a wide absorption band in the NIR region associated with LSPR is clearly observed in the UV/Vis/NIR spectrum of Cu₃SnS₄ NFs. The natural excitation of Cu₃SnS₄ LSPRs in the NIR paves the way for the employment of Cu₃SnS₄ NFs as SERS substrate for enhanced signals of Raman imaging. Here, we set out to explore the possibility of utilizing Cu₃SnS₄ NFs as a SERS substrate for the determination of bacteria content. *E. coli* was used as the model bacteria and tagged with Raman reporter molecules of 3,3'-diethylthiatricarbocyanine iodide (DTTC), followed by the immobilizing of Cu₃SnS₄ NFs (designated as *E. coli*-DTTC-Cu₃SnS₄). The as-prepared *E. coli*-DTTC-Cu₃SnS₄ is illustrated in **Figure 8A**. The EDS analysis of the *E. coli*-DTTC-Cu₃SnS₄ showed well-merged element images of C, N, O, P, Cu, Sn, and S elements, confirming the presence of both DTTC and Cu₃SnS₄ on the bacteria. The *E. coli*-DTTC-Cu₃SnS₄ were subsequently exposed to a 785 nm laser with 10 mW laser power, 5 s acquisition time, and a 50×object lens. Significant enhancement of characteristic Raman signals of the DTTC molecule around 507, 621, 784, 848, 1082, 1134, and 1248 cm⁻¹ was observed after the coupling of Cu₃SnS₄ NFs^[48, 49], while negligible Raman signal was captured in equivalent *E. coli*-DTTC without Cu₃SnS₄ nanostructure (Figure 8C). This result clearly demonstrates the possibility of Cu₃SnS₄ NFs as SERS substrate for the enhancement of Raman probe signals. As can be seen from the UV/Vis/NIR spectrum of *E. coli*-DTTC-Cu₃SnS₄ (Figure 8D and Figure S14), the LSPR peak of *E. coli*-DTTC-Cu₃SnS₄ was in proximity with the wavelength of the excitation laser for SERS imaging (785 nm). The enhancement thus could be attributed to the LSPR on the Cu₃SnS₄ NFs under the excitation of 785 nm laser beam, which strengthened local electromagnetic field and led to enhanced Raman probe signals^[50]. We subsequently demonstrate the high sensitivity of utilizing Cu₃SnS₄ NFs for SERS based *E. coli* detection. A series of *E. coli* tagged with DTTC at concentrations from 10⁸ CFU mL⁻¹ to 10³ CFU mL⁻¹ were coupled with Cu₃SnS₄ NFs, followed by subjection to SERS detection. As shown in Figure 8E and Figure S15, the SERS labeled bacteria with different cell counts from 10⁸ CFU mL⁻¹ to 10⁴ CFU mL⁻¹ could be clearly delineated with low signal-to-background ratio. Using the Raman shift of DTTC molecule at 507 cm⁻¹ for detection, *E. coli* could be detected at a minimal concentration of 10⁴ CFU mL⁻¹. Figure 8F

displays the intensity of the SERS peak at 507 cm^{-1} as a function of logarithmic concentrations of *E. coli*-DTTC-Cu₃SnS₄. A linear dependence was found with concentrations of *E. coli*-DTTC-Cu₃SnS₄ ranging from 10^4 CFU mL^{-1} to 10^8 CFU mL^{-1} , corresponding to doses of Cu₃SnS₄ ranging from $75.5\text{ }\mu\text{M}$ to $325.7\text{ }\mu\text{M}$ (Figure S16). Compared with common noble metals (Ag and Au) nanostructure-based substrates, the fabrication procedure of Cu-based Cu₃SnS₄ NFs is facile and low-cost, thus representing a promising active substrate for SERS based bacteria detection.

Conclusions

In conclusion, photo-activatable Cu₃SnS₄ NFs were prepared for advanced antibacterial therapy by inducing efficient bacteria eradication and accelerated wound healing. The Cu₃SnS₄ NFs could be activated by visible light, leading to effective overproduction of ROS in bacterial cells. Besides, the high photothermal conversion efficiency of Cu₃SnS₄ NFs induced NIR light (808 nm) controlled hyperthermia in bacteria. Importantly, the electrostatic interaction between the positively charged Cu₃SnS₄ NFs and the negatively charged bacteria facilitated the physical contact mediated bacteria killing. Consequently, the physical contact and ROS mediated cellular oxidative damage as well as the NIR mediated photothermal disruption of bacterial membranes played a synergistic role in the efficient eradication of both *E. coli* and MRSA *in vitro* and *in vivo*. On the other hand, the exogenous ions metabolism from the Cu₃SnS₄ NFs significantly up-regulated the expression of HIF-1 α , CD31 and VEGF, leading to increased formation of granulation tissue, collagen synthesis and eventually improved wound healing. Additionally, the Cu₃SnS₄ NFs can be used as an active SERS imaging substrate for SERS-labeled bacteria detection *in vitro*. The sensitive bacteria detection and the solar-driven broad-spectrum antibacterial therapeutic effects as well as the high biocompatibility and therapeutic biosafety endow Cu₃SnS₄ NFs with potentiality for future clinical transformation.

Methods

Materials

Reagents and kits

Copper acetate hydrate (CuAc₂·H₂O), stannic chloride pentahydrate (SnCl₄·5H₂O), hydrogen peroxide (H₂O₂, 30 wt%), thioacetamide (TAA), and N,N-dimethylformamide (DMF) were obtained from Sinopharm Chemical Reagent Co., Ltd. Sodium azide (NaN₃), t-butanol (t-BuOH), benzoquinone, and methylene blue (MB) were purchased from Aladdin Chemical Reagent Co., Ltd. 5,5-dimethyl-1-pyrroline N-oxide (DMPO) and 2,2,6,6-tetramethylpiperidine-1-oxyl (TEMPO) were bought from Adamas Reagent, Ltd. All reagents were purchased as received and used without any further purification.

Preparation and characterization of Cu₃SnS₄ NFs

The Cu₃SnS₄ NFs were prepared by a facile solvothermal strategy. In a typical synthesis, 0.06 mmol CuAc₂·H₂O, 0.04 mmol SnCl₄·5H₂O and 0.08 mmol thioacetamide (TAA) were mixed in 10 ml N,N-dimethylformamide (DMF). The mixture was purged with argon and stirred for 2 h under 140 °C. Then, the reaction mixture was transferred to a stainless-steel autoclave and the reaction was processed at 220 °C for 12 h. After completing the reaction, the mixture was naturally cooled to room temperature and centrifuged at 5000 rpm for 10 min. The precipitate was washed with acetone and deionized water to remove by-products. The obtained black powder was dried at 80 °C for 12 h and used for further characterization.

Characterization

Transmission electron microscopy (TEM), high resolution-TEM (HRTEM), energy dispersive X-ray spectroscopy (EDS), and the corresponding element mapping analyses were conducted on a JEM-2100F electron microscope. Zeta potential was determined on Malvern Zetasizer Nanoseries (Nano ZS90). X-ray photoelectron spectroscopy (XPS) was acquired on an Axis Ultra DLD spectrometer (Kratos, UK). UV-visible (UV/Vis) absorbance spectra were obtained on a UV-3101 Shimadzu spectroscope. The quantitative elemental analysis was carried out on an inductively coupled plasma optical emission spectrometer (ICP-OES, Agilent 700 Series, USA). Powder X-ray diffraction (XRD) pattern was tested on a Rigaku Ultima IV diffractometer. The electron paramagnetic resonance (EPR) was conducted on a Bruker EMXplus X-band EPR.

The photocatalysis mediated ROS generation from Cu₃SnS₄ NFs

The photocatalysis mediated ROS generation was evaluated using the methylene blue (MB) probe. Briefly, 4 mL of methylene blue (MB, 10 µg mL⁻¹) aqueous solution was added to 6 mL of the aqueous solution containing 0.6 mg of Cu₃SnS₄ NFs and shaken slightly under light. 0.5 mL of the reaction suspension was then taken out, diluted with water, and detected by a UV/Vis spectrometer at 664 nm periodically. The MB degradation process was also photographed. To investigate the Cu ions mediated Fenton-like reaction, 1 mL of H₂O₂ aqueous solution (1 mM) was immediately added to the above solution and the MB degradation was evaluated with a similar procedure.

Additionally, using DMPO and TEMPO as spin probes, the photocatalysis mediated ROS (including •OH, 1O₂, and O₂^{•-}) generation was further detected by electron paramagnetic resonance (EPR). Typically, 0.1 mg of Cu₃SnS₄ NFs were added to 10 mL of deionized water under dark conditions. The suspension was then exposed to visible light irradiation and the EPR signal of the complex of •OH, 1O₂, and O₂^{•-} with the probes was captured periodically (0, 1 and 2 min).

The NIR mediated hyperthermia of Cu₃SnS₄ NFs

The NIR mediated hyperthermia and the photothermal efficiency of the Cu₃SnS₄ NFs were investigated using an 808 nm fiber-coupled laser system. Briefly, different concentrations of Cu₃SnS₄ dispersions (0, 25, 50, 100, 200 and 400 µg mL⁻¹) were irradiated by an 808 nm fiber-coupled laser system for different times (0, 2, 4, 6, 8 and 10 min) at varied power density (0, 1, 1.5, 2 and 2.5 W cm⁻²). The temperature of the suspensions was recorded every 50 sec with an IR camera to analyze the temperature elevation tendency. The photothermal stability of Cu₃SnS₄ NFs was evaluated by turning on the NIR laser (808 nm, 2.0 W cm⁻²) for 10 min and then off until the dispersions reached room temperature periodically. Nine circulations were recorded.

The photothermal conversion efficiency (η) was calculated using the following equations:

$$\eta = \frac{hS(T_{Max} - T_{Surr}) - Q_{Dis}}{I(1 - 10^{-A_{808}})}$$
$$hS = \frac{m_D C_D}{\tau_s}$$

In these equations, m_D represents the solution mass and equals to 0.2 g, while $c_D = 4.2$ J/g is the heat capacity of water. $T_{MAX} = 42.15$ °C and $T_{Surr} = 25$ °C are the maximum temperature of the NFs and the water during the irradiation process, respectively. Q_{Dis} is associated with the light absorbance of the solvent, which approximately equals to 0. τ_s is the irradiation time during the temperature rise and equals to 195.5 s. I is the laser power and equals to 2.0 W cm⁻². $A_{808} = 0.47$ is the absorbance of the NFs at 808 nm. The photothermal conversion efficiency was thus calculated to be 55.7%.

The Cu ions released from the Cu₃SnS₄ NFs were investigated by ICP-OES analysis. Typically, 0.5 mg of Cu₃SnS₄ NFs were added to 10 mL of deionized water under dark conditions at room temperature. The Cu ions release process was performed on a shaking table at a shaking speed of 180 rpm. At each time point, 1 mL of the supernate was taken out, filtrated, diluted, and measured by ICP-OES. To investigate the NIR mediated Cu ions release, the suspension was exposed to NIR irradiation (808 nm, 2.0 W cm⁻²) for 10 min.

In vitro cytotoxicity of Cu₃SnS₄ NFs

Human umbilical vein endothelial cells (HUVECs) and mouse fibroblast cells (L929) were obtained from the China Center of Industrial Culture Collection. Cells were seeded separately into 96-well plates at 1×10^6 cells mL⁻¹. The cells were incubated in α -MEM with 10 % FBS at 37 °C in 5% CO₂ atmosphere. After 24 h, the original media was removed, and α -MEM containing a diverse concentration of Cu₃SnS₄ NFs (0, 10, 25, 50, 100 µg mL⁻¹) was added to the plates. Cytotoxicity was detected after 24 h and 48 h co-culture using the MTT method. All wells to be detected were washed with PBS for three times, after which MTT

solution (100 μL , 0.5 mg mL^{-1}) was added to each well and further incubated for 4 h at 37 °C. The optical density (OD) of each solution was tested at 492 nm using an ELX-800 absorbance microplate reader.

In vitro bacterial cell culture

Gram-negative E. Coli (ATCC 25922) and Gram-positive methicillin-resistant S. aureus (MRSA, ATCC 43300) were obtained from American Type Culture Collection(ATCC). E. coli (ATCC 25922) and MRSA (ATCC 43300) were initially seeded on solid Luria-Bertani Broth medium with streak plate method. After being cultured at 36 °C for 24 h, we collected a single bacterial colony and immersed it into 10 mL of liquid Luria-Bertani Broth medium separately for further cultivation. The centrifuge tubes were placed in a shaking incubator at 100 rpm at 30 °C for 20 h. Cells were then centrifuged (5000 rpm, 10 min, 4 °C) and washed with PBS for three times before use.

The evaluation of antibacterial activity of Cu₃SnS₄ NFs in Vitro

The antibacterial probability of Cu₃SnS₄ NFs was measured with the spread plate method. The solution was concentrated using a centrifuge (5000 rpm, 10 min, 4 °C) and the supernatant was removed. Next, the pellets were resuspended and diluted at a density of 1×10^5 CFU mL^{-1} with PBS (pH 6.0) containing Cu₃SnS₄ NFs at 100 $\mu\text{g mL}^{-1}$ and 0 $\mu\text{g mL}^{-1}$, according to the optical density (OD) value tested at 650 nm. Each concentration of solution underwent various disposal: I. Control: A suspension containing 0 $\mu\text{g mL}^{-1}$ of Cu₃SnS₄ NFs, irradiated with steady light. II. A suspension containing 0 $\mu\text{g mL}^{-1}$ of Cu₃SnS₄ NFs, irradiated with steady light and NIR laser (808 nm, 2 W cm^{-2} , 10 min). III. A suspension containing 100 $\mu\text{g mL}^{-1}$ of Cu₃SnS₄ NFs, irradiated with steady light. IV: A suspension containing 100 $\mu\text{g mL}^{-1}$ of Cu₃SnS₄ NFs, irradiated with steady light and NIR laser (808 nm, 2 W cm^{-2} , 10 min). After the procedure, 100 μl of each diluted suspension was spread onto the solid Luria-Bertani Broth medium, incubated at 37 °C in 5% CO₂ overnight. The number of bacterial colonies was then counted.

In vitro fluorescence live/dead staining of bacteria

The bacterial suspensions were prepared in different methods : I. PBS. II. PBS + NIR laser (808 nm, 2 W cm^{-2} , 10 min). III. Cu₃SnS₄ NFs (100 $\mu\text{g mL}^{-1}$). IV. Cu₃SnS₄ NFs (100 $\mu\text{g mL}^{-1}$) + NIR laser (808 nm, 2 W cm^{-2} , 10 min). Before staining, the supernatant containing bacterial cells was collected and centrifuged to remove Cu₃SnS₄ NFs. The supernatant was also discarded to remove nucleic acids or other media components that might decrease staining efficiency. Then we resuspended the pellets with sterile water containing 0.85% NaCl, SYTO9 (10 μM) and PI (10 μM). The suspension was incubated in the dark for 15 min. The stained cells were transferred to confocal dishes. Fluorescent images of the live (green fluorescent) and dead (red fluorescent) cells were obtained using an Olympus confocal laser scanning microscope.

Morphology observation of bacteria by bio-SEM

After the anti-bacteria test, cell morphology images were acquired by SEM scanning. The bacterial suspensions: I. PBS. II. PBS + NIR laser (808 nm, 2 W cm⁻², 10 min). III. Cu₃SnS₄ NFs (100 µg mL⁻¹). IV. Cu₃SnS₄ NFs (100 µg mL⁻¹) + NIR laser (808 nm, 2 W cm⁻², 10 min) were fixed with 2.5 % glutaraldehyde overnight at 4 °C. All samples were centrifuged and resuspended with PB (0.1 M) for four times. Then all samples were fixed with osmic acid (1 %, pH 7.3) for 1 hour. Before dehydration, samples were washed with PB (0.1 M) and ultrapure water for 2 times. Graded alcohol (30 %, 50 %, 60 %, 70 %, 80 %, 90 %, 100 %, 100 %, and 100 %) was applied to dehydrate the bacteria. During each procedure, the pellets were mixed with solution thoroughly for 10 minutes. All samples were dried using the supercritical CO₂ drying technology. The bacteria morphology was visualized using bio-SEM.

Animals

Male ICR mice aged 5 weeks were obtained from Shanghai Super - B&K laboratory animal Corp. Ltd. The Institutional Animal Care and Use Committee of Shanghai Ninth People's Hospital, Shanghai Jiao Tong University School of Medicine approved all the animal study protocols. All animal experiments were carried out in agreement with the guidelines of Shanghai Laboratory Animal Research Center.

In vivo wound disinfection and healing assay

The ICR mice were divided into four groups, and each group consists of four mice. All mice were raised in cages under the same condition. First, the mice were injected with 5% chloral hydrate in the abdominal cavity. After anesthesia took effect, a circular wound in 6 mm was prepared on the back of each mouse with a skin punch. One day after the wound was created, 50 µL of MRSA solution (2 × 10⁸ CFU mL⁻¹) was dropped into each wound to construct the wound healing model. According to the grouping, various treatments were operated: I. PBS. II. PBS + NIR laser (808 nm, 1.0 W cm⁻², 10 min). III. Cu₃SnS₄ NFs (100 µg mL⁻¹). IV. Cu₃SnS₄ NFs (100 µg mL⁻¹) + NIR laser (808 nm, 1.0 W cm⁻², 10 min). Meantime, an IR camera was deployed to record thermal images. Body weights and wound sizes were recorded every 2 days post wounding until all mice were sacrificed on the 8th day after treatment. Meanwhile, in vivo biosafety and wound healing was investigated through HE staining, masson's trichrome staining, and immunofluorescence staining (CD31, VEGF), utilizing skin tissues and main organs (liver, spleen, lung, and kidney) harvested. For the Western blot analyses, formalin-fixed, paraffin-embedded (FFPE) skin wound samples were sectioned at a thickness of 10 µm. After sections were dewaxed by adding 500 µL of octane and vigorously shaken for 10 s, 750 µL methanol was added and shaken for another 10 s. Samples were then centrifuged (15,000 g, 10 min, 4 °C) to remove the upper suspension, and pellets were dried for 5 min. 50 µL of lysis buffer containing 20 mM Tris-HCl (pH 7.4) and 2% SDS was added, followed by heating at 100 °C for 20 min and 60 °C for 2 h. Samples were then collected and went through western blot assay. Expression variation of CD31 and HIF-1α was tested.

Declarations

Acknowledgments

We thank We thank the Instrumental Analysis Center of Shanghai Jiao Tong University for materials testing.

Author's contributions

YH, JF and YY designed the plan of the experiments. YY and JF performed the synthesis and characterization experiments of the material. YY and CW performed the *in vitro* experiments. YY, JF, and JL participated in the *in vivo* experiments. NW, JL, YZ and JZ contributed to data analysis. YY and JF drafted the manuscript. YY, JF and YH contributed to the manuscript preparation. All authors read and approved the final manuscript.

Funding

We acknowledge the financial support from the National Natural Science Foundation of China (Nos. 81801821, 81972058, and 51872313), and Shanghai Municipal Key Clinical Specialty (No. shslczdzk06701).

Availability of data and materials

All data generated or analyzed during this study are included in this article.

Consent for publication

All authors agree to be published.

Competing interests

The authors declare that they have no competing interests.

Author details

¹ Shanghai Key Laboratory of Orthopaedic Implant, Department of Orthopaedic Surgery, Shanghai Ninth People's Hospital, Shanghai Jiao Tong University School of Medicine, Shanghai 200011, China. ² Clinical and Translational Research Center for 3D Printing Technology, Shanghai Ninth People's Hospital, Shanghai Jiao Tong University School of Medicine, Shanghai 200011, China. ³ Department of Orthopedics, The Second Affiliated Hospital of Harbin Medical University, Harbin 150081, China. ⁴ Shanghai Electrochemical Energy Devices Research Center, School of Chemistry and Chemical Engineering and State Key Laboratory of Metal Matrix Composites, Shanghai Jiao Tong University, Shanghai 200240, China. ⁵ Key Laboratory of Inorganic Coating Materials, Shanghai Institute of Ceramics, Chinese Academy of Sciences, Shanghai 200050, China.

References

1. Levy SB, Marshall B. Antibacterial resistance worldwide: causes, challenges and responses. *Nat Med*. 2004;10:122–9.
2. Wang CY, Makvandi P, Zare EN, Tay FR, Niu LN. Advances in antimicrobial organic and inorganic nanocompounds in biomedicine. *Adv Therap*. 2020;3:2000024.
3. Jiao Y, Niu LN, Ma S, Li J, Tay FR, Chen JH. Quaternary ammonium-based biomedical materials: State-of-the-art, toxicological aspects and antimicrobial resistance. *Prog Polym Sci*. 2017;71:53–90.
4. Ding XK, Duan S, Ding XJ, Liu RH, Xu FJ. Versatile antibacterial materials: An emerging arsenal for combatting bacterial pathogens. *Adv Funct Mater*. 2018;28:1802140.
5. Li X, Bai HT, Yang YC, Yoon J, Wang S, Zhang X. Supramolecular antibacterial materials for combatting antibiotic resistance. *Adv Mater*. 2019;31:1805092.
6. Hu XL, Shang Y, Yan KC, Sedgwick AC, Gan HQ, Chen GR, He XP, James TD, Chen DJ. Low-dimensional nanomaterials for antibacterial applications. *J Mater Chem B*. 2021;9:3640–61.
7. You JH, Guo YZ, Guo R, Liu XW. A review of visible light-active photocatalysts for water disinfection: Features and prospects. *Chem Eng J*. 2019;373:624–41.
8. Zhou ZL, Li B, Liu XM, Li ZY, Zhu SL, Liang YQ, Cui ZD, Wu SL. Recent progress in photocatalytic antibacterial. *ACS Appl Bio Mater*. 2021;4:3909–36.
9. Wang WJ, Li GY, Xia DH, An TC, Zhao HJ, Wong PK. Photocatalytic nanomaterials for solar-driven bacterial inactivation: recent progress and challenges. *Environ Sci-Nano*. 2017;4:782–99.
10. Li Y, Liu XM, Tan L, Cui ZD, Yang XJ, Zheng YF, Yeung KWK, Chu PK, Wu SL. Rapid sterilization and accelerated wound healing using Zn^{2+} and graphene oxide modified $g-C_3N_4$ under dual light irradiation. *Adv Funct Mater*. 2018;28:1800299.
11. Zhang Y, Sun PP, Zhang L, Wang ZZ, Wang FM, Dong K, Liu Z, Ren JS, Qu XG. Silver-infused porphyrinic metal-organic framework: Surface-adaptive, on-demand nanoplatform for synergistic bacteria killing and wound disinfection. *Adv Funct Mater*. 2019;29:1808594.
12. Lambeth JD. Nox enzymes and the biology of reactive oxygen. *Nat Rev Immunol*. 2004;4:181–9.
13. Ren YW, Liu HP, Liu XM, Zheng YF, Li ZY, Li CY, Yeung KWK, Zhu SL, Liang YQ, Cui ZD, Wu SL. Photoresponsive materials for antibacterial applications. *Cell Rep Phys Sci*. 2020;1:100245.
14. Yang R, Song G, Wang L, Yang Z, Zhang J, Zhang X, Wang S, Ding L, Ren N, Wang A, Yu X. Full solar-spectrum-driven antibacterial therapy over hierarchical Sn_3O_4 /PDINH with enhanced photocatalytic activity. *Small*. 2021;17:2102744.
15. Makabenta JMV, Nabawy A, Li CH, Schmidt-Malan S, Patel R, Rotello VM. Nanomaterial-based therapeutics for antibiotic-resistant bacterial infections. *Nat Rev Microbiol*. 2021;19:23–36.
16. Reddy VRM, Pallavolu MR, Guddeti PR, Gedi S, Reddy KKYB, Pejjai B, Kim WK, Kotte TRR, Park C. Review on Cu_2SnS_3 , Cu_3SnS_4 , and Cu_4SnS_4 thin films and their photovoltaic performance. *J Ind Eng Chem*. 2019;76:39–74.

17. Munoz-Batista MJ, Fontelles-Carceller O, Ferrer M, Fernandez-Garcia M, Kubacka A. Disinfection capability of Ag/g-C₃N₄ composite photocatalysts under UV and visible light illumination. *Appl Catal B-Environ.* 2016;183:86–95.
18. Han QY, Lau JW, Do HC, Zhang ZJ, Xing BG. Near-infrared light brightens bacterial disinfection: Recent progress and perspectives. *ACS Appl Bio Mater.* 2021;4:3937–61.
19. Wang X, Shi Q, Zha Z, Zhu D, Zheng L, Shi L, Wei X, Lian L, Wu K, Cheng L. Copper single-atom catalysts with photothermal performance and enhanced nanozyme activity for bacteria-infected wound therapy. *Bioact Mater.* 2021;6:4389–401.
20. Tang H, Qu X, Zhang W, Chen X, Zhang S, Xu Y, Yang H, Wang Y, Yang J, Yuan WE, Yue B. Photosensitizer nanodot eliciting immunogenicity for photo-immunologic therapy of postoperative methicillin-resistant staphylococcus aureus infection and secondary recurrence, *Adv. Mater.* <https://doi.org/10.1002/adma.202107300>.
21. Borkow G. Using copper to improve the well-being of the skin. *Curr Chem Biol.* 2014;8:89–102.
22. Lokhande AC, Shelke A, Babar PT, Kim J, Lee DJ, Kim IC, Lokhande CD, Kim JH. Novel antibacterial application of photovoltaic Cu₂SnS₃ (CTS) nanoparticles. *RSC Adv.* 2017;7:33737–44.
23. Ali N, Tsega TT, Cao YC, Abbas S, Li WJ, Iqbal A, Fazal H, Xin ZL, Zai JT, Qian XF. Copper vacancy activated plasmonic Cu_{3-x}SnS₄ for highly efficient photocatalytic hydrogen generation: Broad solar absorption, efficient charge separation and decreased HER overpotential. *Nano Res.* 2021;14:3358–64.
24. Chen FK, Zai JT, Xu M, Qian XF. 3D-hierarchical Cu₃SnS₄ flowerlike microspheres: Controlled synthesis, formation mechanism and photocatalytic activity for H₂ evolution from water. *J Mater Chem A.* 2013;1:4316–23.
25. Hu HM, Liu ZP, Yang BJ, Chen XY, Qian YT. Template-mediated growth of Cu₃SnS₄ nanoshell tubes. *J Cryst Growth.* 2005;284:226–34.
26. Xiong YJ, Xie Y, Du GA, Su HL. From 2D framework to quasi-1D nanomaterial: Preparation, characterization, and formation mechanism of Cu₃SnS₄ nanorods. *Inorg Chem.* 2002;41:2953–9.
27. Fu LH, Wan YL, Qi C, He J, Li CY, Yang C, Xu H, Lin J, Huang P. Nanocatalytic theranostics with glutathione depletion and enhanced reactive oxygen species generation for efficient cancer therapy. *Adv Mater.* 2021;33:2006892.
28. Zhou XR, Zhu Y, Niu QY, Zeng GM, Lai C, Liu SY, Huang DL, Qin L, Liu XG, Li BS, Yi H, Fu YK, Li L, Zhang MM, Zhou CY, Liu JH. New notion of biochar: A review on the mechanism of biochar applications in advanced oxidation processes. *Chem Eng J.* 2021;416:129027.
29. Zhou L, Song W, Chen ZQ, Yin GC. Degradation of organic pollutants in wastewater by bicarbonate-activated hydrogen peroxide with a supported cobalt catalyst. *Environ Sci Technol.* 2013;47:3833–9.
30. Ge L, Chen JW, Lin J, Cai XY. Light-Source-dependent effects of main water constituents on photodegradation of phenicol antibiotics: Mechanism and kinetics. *Environ Sci Technol.* 2009;43:3101–7.

31. Khan A, Zhang KK, Taraqqi-A-Kamal A, Wang XG, Chen Y, Zhang YR. Degradation of antibiotics in aqueous media using manganese nanocatalyst-activated peroxymonosulfate. *J Colloid Interf Sci.* 2021;599:805–18.
32. Yin MC, Li ZS, Kou JH, Zou ZG. Mechanism investigation of visible light-induced degradation in a heterogeneous TiO_2 /Eosin Y/Rhodamine B system. *Environ Sci Technol.* 2009;43:8361–6.
33. Wang LW, Zhang X, Yu X, Gao EN, Shen ZY, Zhang XL, Ge SG, Liu J, Gu ZJ, Chen CY. An all-organic semiconductor C_3N_4 /PDINH heterostructure with advanced antibacterial photocatalytic therapy activity. *Adv Mater.* 2019;31:1901965.
34. Li YW, Ling WD, Han QF, Kim TW, Shi WZ. Localized surface plasmon resonances and its related defects in orthorhombic Cu_3SnS_4 nanocrystals. *J Alloy Compd.* 2015;633:347–52.
35. Zhang X, Zhang G, Chai M, Yao X, Chen W, Chu PK. Synergistic antibacterial activity of physical-chemical multi-mechanism by TiO_2 nanorod arrays for safe biofilm eradication on implant. *Bioact Mater.* 2021;6:12–25.
36. Guillamat-Prats R. The role of MSC in wound healing, scarring and regeneration. *Cells.* 2021;10:1729.
37. Dong CH, Feng W, Xu WW, Yu LD, Xiang H, Chen Y, Zhou JQ. The coppery age: Copper (Cu)-involved nanotheranostics. *Adv Sci.* 2020;7:2001549.
38. Xiao JS, Chen SY, Yi J, Zhang HF, Ameer GA. A cooperative copper metal-organic framework-hydrogel system improves wound healing in diabetes. *Adv Funct Mater.* 2017;27:1604872.
39. Rucker RB, Kosonen T, Clegg MS, Mitchell AE, Rucker BR, Uriu-Hare JY, Keen CL. Copper, lysyl oxidase, and extracellular matrix protein cross-linking. *Am J Clin Nutr.* 1998;67:996s–1002s.
40. Li Y, Fu R, Duan Z, Zhu C, Fan D. Construction of multifunctional hydrogel based on the tannic acid-metal coating decorated MoS_2 dual nanozyme for bacteria-infected wound healing. *Bioact Mater.* 2022;9:461–74.
41. Valarmathi MT, Davis JM, Yost MJ, Goodwin RL, Potts JD. A three-dimensional model of vasculogenesis. *Biomaterials.* 2009;30:1098–112.
42. Fan W, Crawford R, Xiao Y. Enhancing in vivo vascularized bone formation by cobalt chloride-treated bone marrow stromal cells in a tissue engineered periosteum model. *Biomaterials.* 2010;31:3580–9.
43. Ahluwalia A, Tarnawski AS. Critical role of hypoxia sensor - HIF-1 α in VEGF gene activation. Implications for angiogenesis and tissue injury healing. *Curr Med Chem.* 2012;19:90–7.
44. Heun Y, Pogoda K, Anton M, Pircher J, Pfeifer A, Woernle M, Ribeiro A, Kameritsch P, Mykhaylyk O, Plank C, Kroetz F, Pohl U, Mannell H. HIF-1 α dependent wound healing angiogenesis in vivo can be controlled by site-specific lentiviral magnetic targeting of SHP-2. *Mol Ther.* 2017;25:1616–27.
45. Perez-Jimenez AI, Lyu D, Lu ZX, Liu GK, Ren RB. Surface-enhanced Raman spectroscopy: benefits, trade-offs and future developments. *Chem Sci.* 2020;11:4563–77.
46. Zhou X, Hu ZW, Yang DT, Xie SX, Jiang ZJ, Niessner R, Haisch C, Zhou HB, Sun PH. Bacteria detection: From powerful SERS to its advanced compatible techniques. *Adv Sci.* 2020;7:2001739.

47. Xu J, Liu N, Wu D, Gao Z, Song YY, Schmuki P. Upconversion nanoparticle-assisted payload delivery from TiO_2 under near-infrared light irradiation for bacterial inactivation. *ACS Nano*. 2020;14:337–46.
48. Qiu Y, Lin M, Chen G, Fan C, Li M, Gu X, Cong S, Zhao Z, Fu L, Fang X, Xiao Z. Photodegradable CuS SERS probes for intraoperative residual tumor detection, ablation, and self-clearance. *ACS Appl Mater Inter*. 2019;11:23436–44.
49. He J, Qiao Y, Zhang H, Zhao J, Li W, Xie T, Zhong D, Wei Q, Hua S, Yu Y, Yao K, Santos HA, Zhou M. Gold-silver nanoshells promote wound healing from drug-resistant bacteria infection and enable monitoring via surface-enhanced Raman scattering imaging. *Biomaterials*. 2020;234:119763.
50. Hsu YK, Chen ZB, Lin YC, Chen YC, Chen SY, Lin YG. Room-temperature fabrication of Cu nanobrushes as an effective surface-enhanced Raman scattering substrate. *Crystrngcomm*. 2016;18:8284–90.

Figures

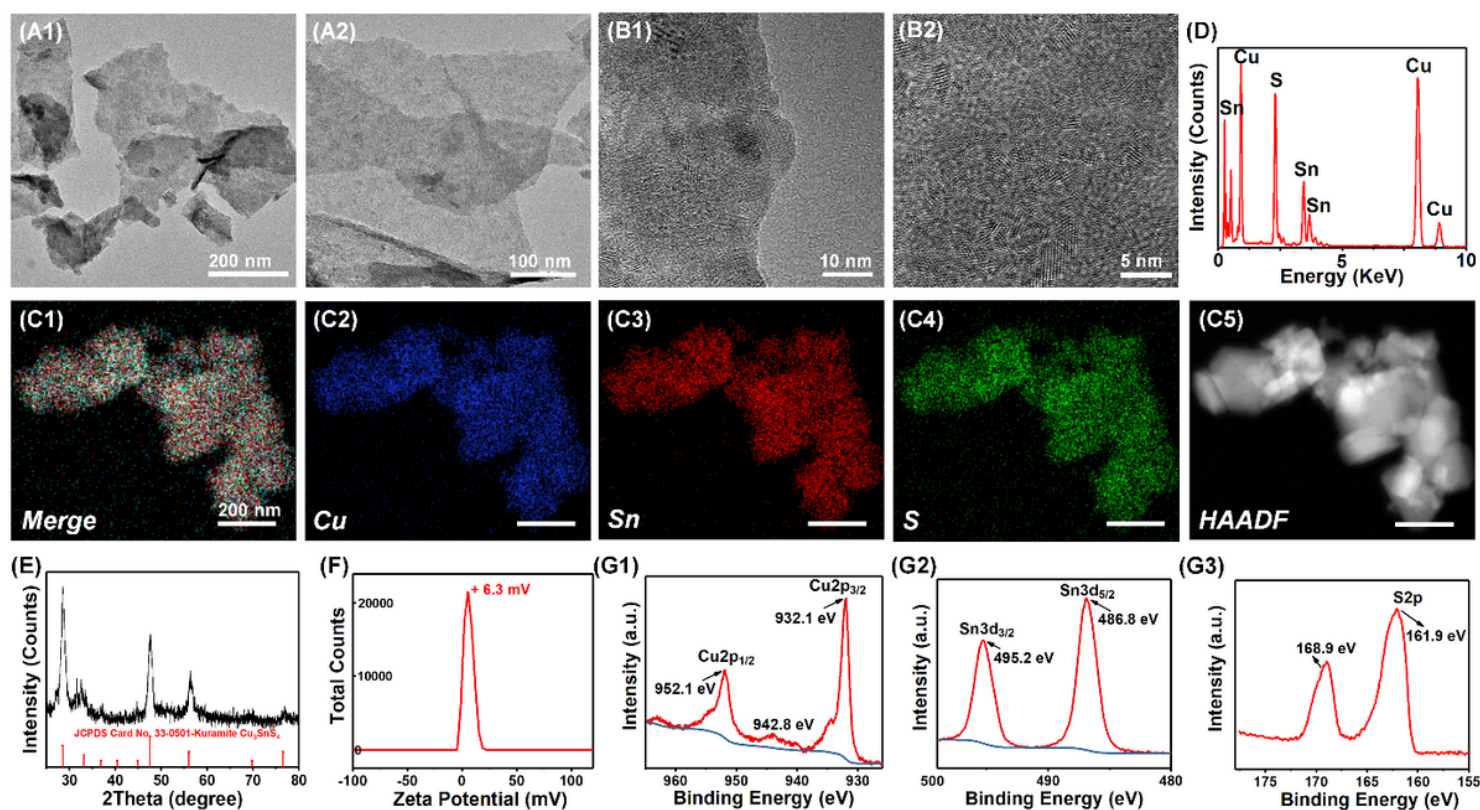


Figure 1

Characterization of as-prepared Cu_3SnS_4 NFs. (A, B) TEM images of Cu_3SnS_4 NFs. (C) Element mappings of Cu, Sn and S elements in Cu_3SnS_4 . (D) EDS of the Cu_3SnS_4 NFs. (E) XRD pattern of the as-prepared Cu_3SnS_4 and the standard JCPDS card No. 33-0501. (F) Zeta potential of the Cu_3SnS_4 . (G) XPS analyses of the Cu_3SnS_4 .

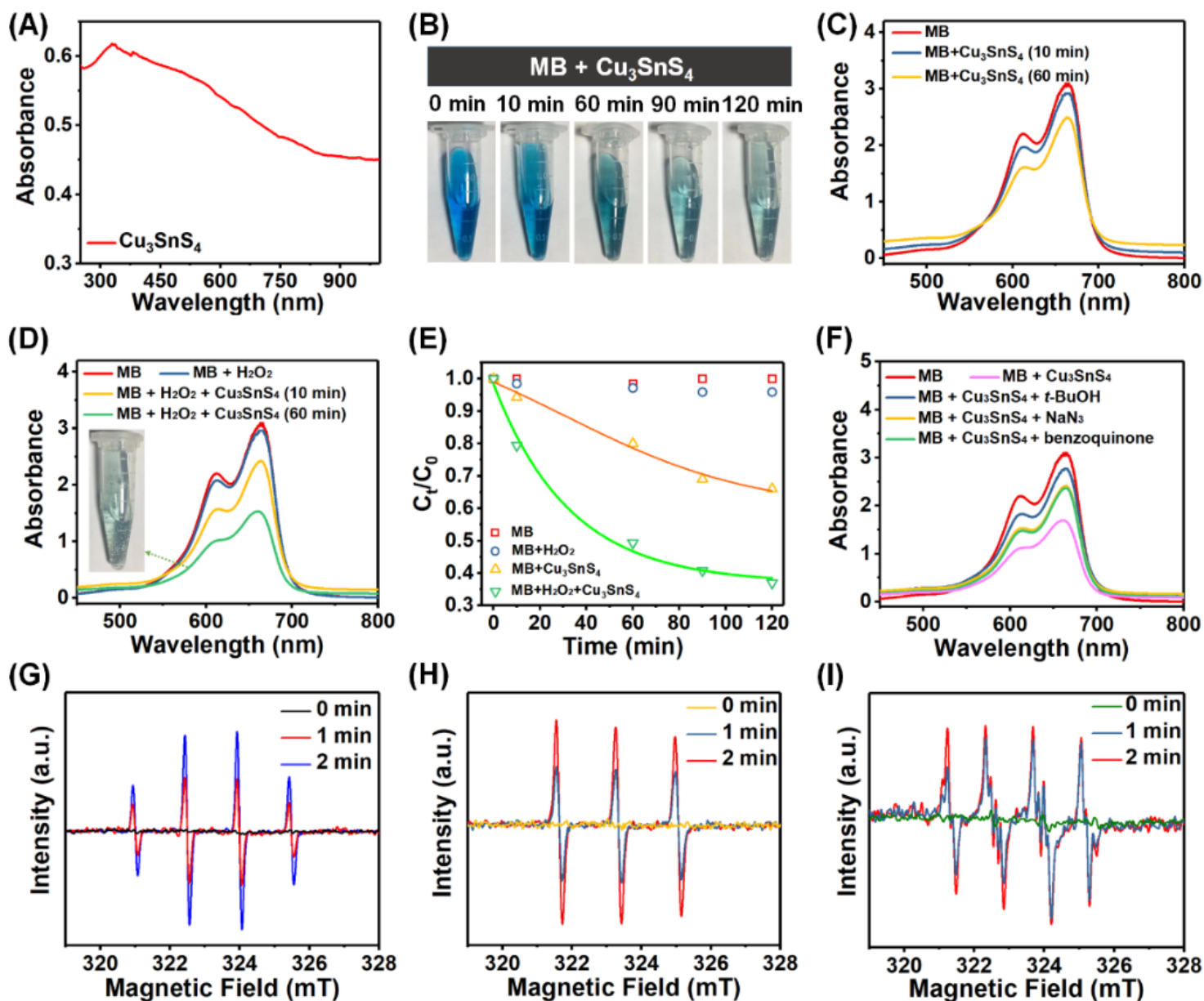


Figure 2

(A) The UV/Vis/NIR absorption spectrum of the Cu_3SnS_4 NFs. (B) Photographs of the Cu_3SnS_4 mediated and time-dependent degradation of MB. (C) Time-dependent UV/Vis absorption spectra of MB solution after incubation with Cu_3SnS_4 under visible light irradiation. (D) Time-dependent UV/Vis absorption spectra of MB solution after incubation with Cu_3SnS_4 and/or H_2O_2 under visible light irradiation. (E) Time-dependent concentration change of MB after incubation with Cu_3SnS_4 and/or H_2O_2 . (F) UV/Vis absorption spectra of MB solution after incubation with Cu_3SnS_4 in the presence of $t\text{-BuOH}$, NaN_3 , or benzoquinone, demonstrating the influence of $t\text{-BuOH}$, NaN_3 , and benzoquinone on the Cu_3SnS_4 -activated MB degradation. (G-I) EPR spectra of G) $\cdot\text{OH}$, H) $^1\text{O}_2$, and I) $\text{O}_2^{\cdot-}$ upon dispersion of Cu_3SnS_4 into deionized water under visible light irradiation for different times.

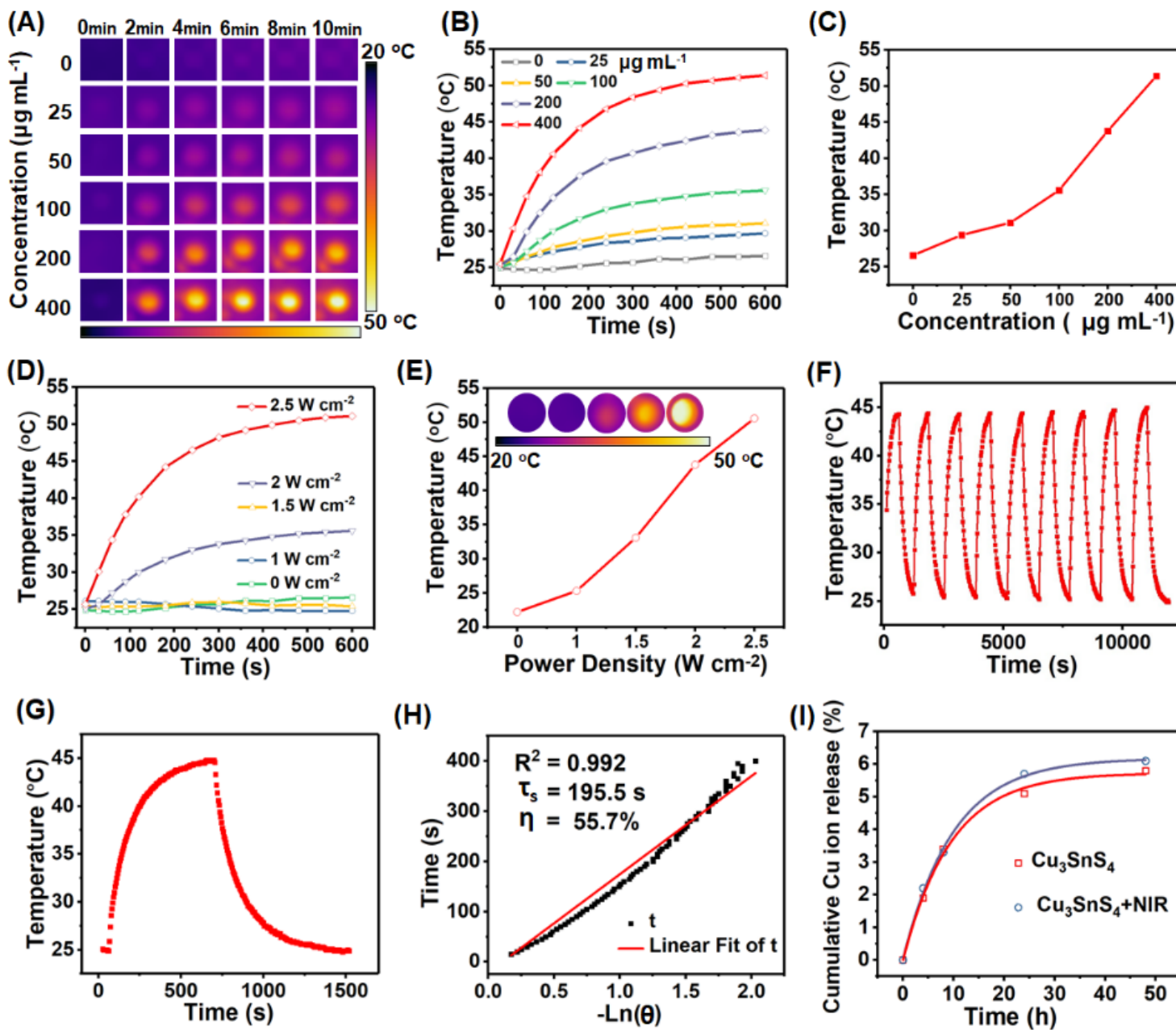


Figure 3

(A-C) Infrared thermal images and corresponding photothermal heating curves of pure water and aqueous dispersions of Cu_3SnS_4 at different Cu_3SnS_4 concentrations under continuous irradiation by a 808 nm laser with a power density of 2.5 W cm^{-2} . (D, E) Photothermal heating curves of aqueous dispersions of Cu_3SnS_4 by a 808 nm laser with varied power density. (F) Temperature changes of Cu_3SnS_4 aqueous dispersions over nine cycles of irradiation/cooling processes. (G) The temperature profile of Cu_3SnS_4 aqueous dispersions irradiated with a 808-nm laser, followed by natural cooling after the laser was turned off. (H) Determination of the system time constant using linear regression of the

cooling profile shown in (G). (I) Cu ions release from the Cu_3SnS_4 in PBS (pH 7.4) in the presence or absence of the NIR irradiation.

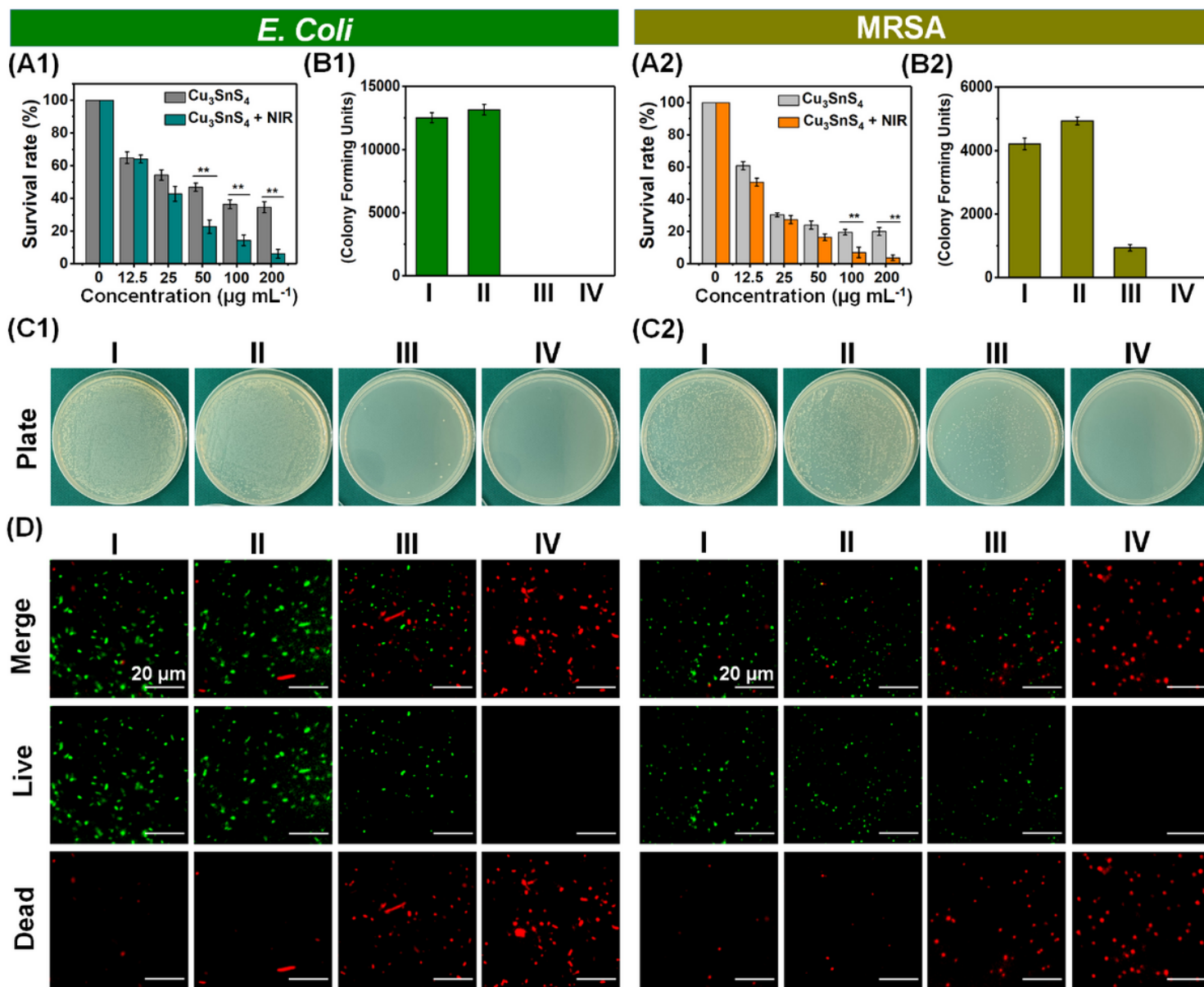


Figure 4

(A) Growth survival of (A1) *E. coli* and (A2) MRSA bacteria. Data are presented as means \pm SDs ($n = 6$). * $p < 0.05$, ** $p < 0.01$. (B) CFU amount of (B1) *E. coli* and (B2) MRSA bacteria. (C) Photographs of (C1) *E. coli* and (C2) MRSA bacterial colonies formed on lysogeny broth (LB)-agar plates. (D) Representative CLSM images of live/dead staining assay for *E. coli* (left) and MRSA (right) after different treatments *via* SYTO9 (green, viable bacteria) and PI (red, dead bacteria) staining. Group I: control group in the absence of NFs and NIR irradiation; Group II: NIR group with the irradiation of NIR laser (808 nm, 1.5 W cm^{-2} , 10 min) in the absence of NFs; Group III: Cu_3SnS_4 group with the treatment with Cu_3SnS_4 NFs under no laser

irradiation; Group IV: Cu_3SnS_4 + NIR group with the treatment with Cu_3SnS_4 NFs plus NIR irradiation (808 nm, 1.5 W cm^{-2} , 10 min). All groups were exposed to visible light for 20 min.

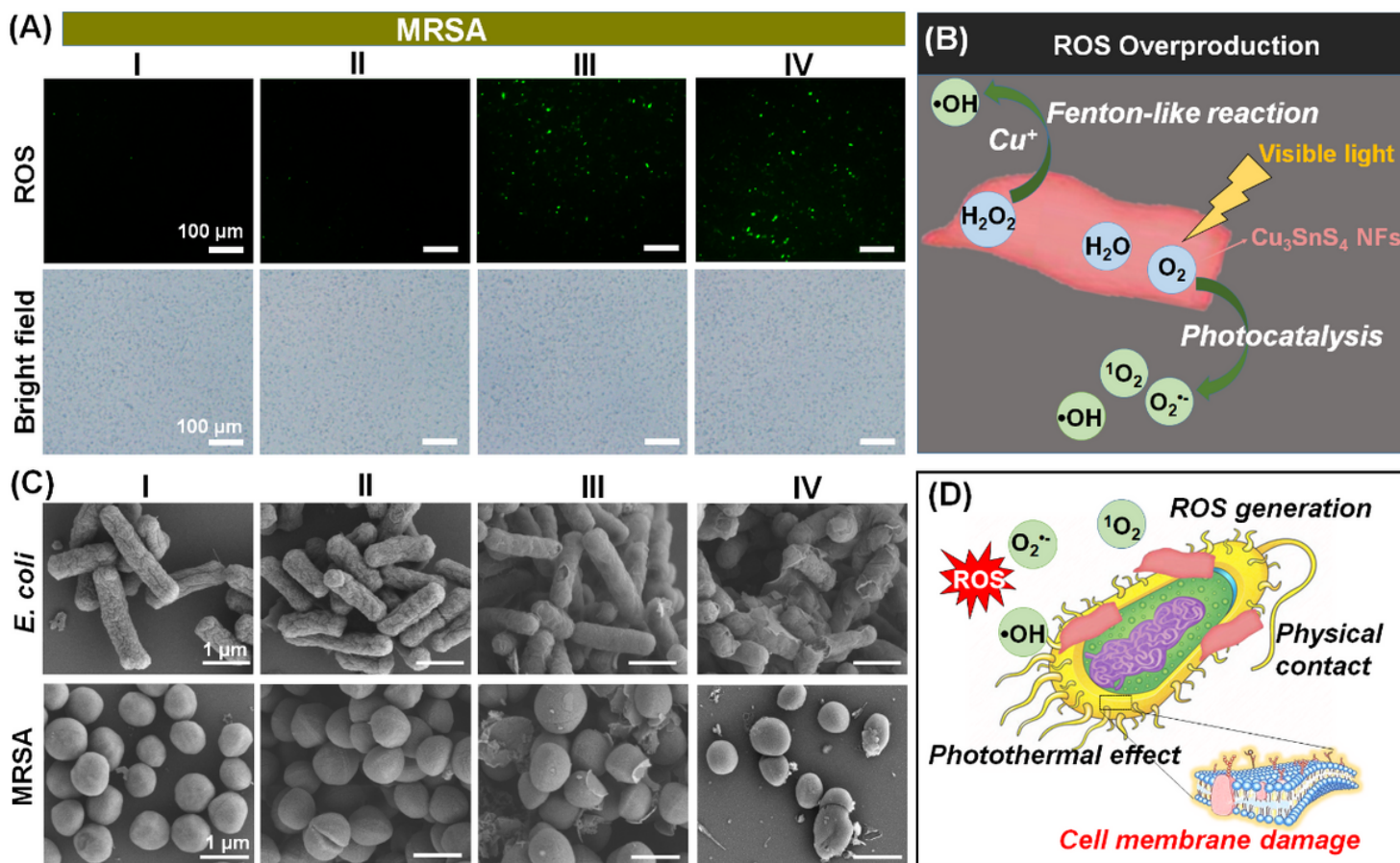


Figure 5

(A) Intracellular ROS level indicated by DCFH-DA fluorescence staining and the corresponding bright-field micrographs after diverse treatments. (B) Scheme of the ROS overproduction induced by the Cu ions mediated Fenton-like reaction and the visible light mediated photocatalytic process. (C) SEM micrographs of *E. coli* and MRSA after different treatments. (D) Scheme of the interaction of the physical contact, ROS generation and photothermal effects, which collaboratively led to the damage of bacteria cell membrane. Group I: control group in the absence of NFs; Group II: NIR group with the irradiation of NIR laser (808 nm, 1.5 W cm^{-2} , 10 min) in the absence of NFs; Group III: Cu_3SnS_4 group with the treatment with Cu_3SnS_4 NFs under no laser irradiation; Group IV: Cu_3SnS_4 + NIR group with the treatment with Cu_3SnS_4 NFs plus NIR irradiation (808 nm, 1.5 W cm^{-2} , 10 min). All groups were exposed to visible light for 20 min.

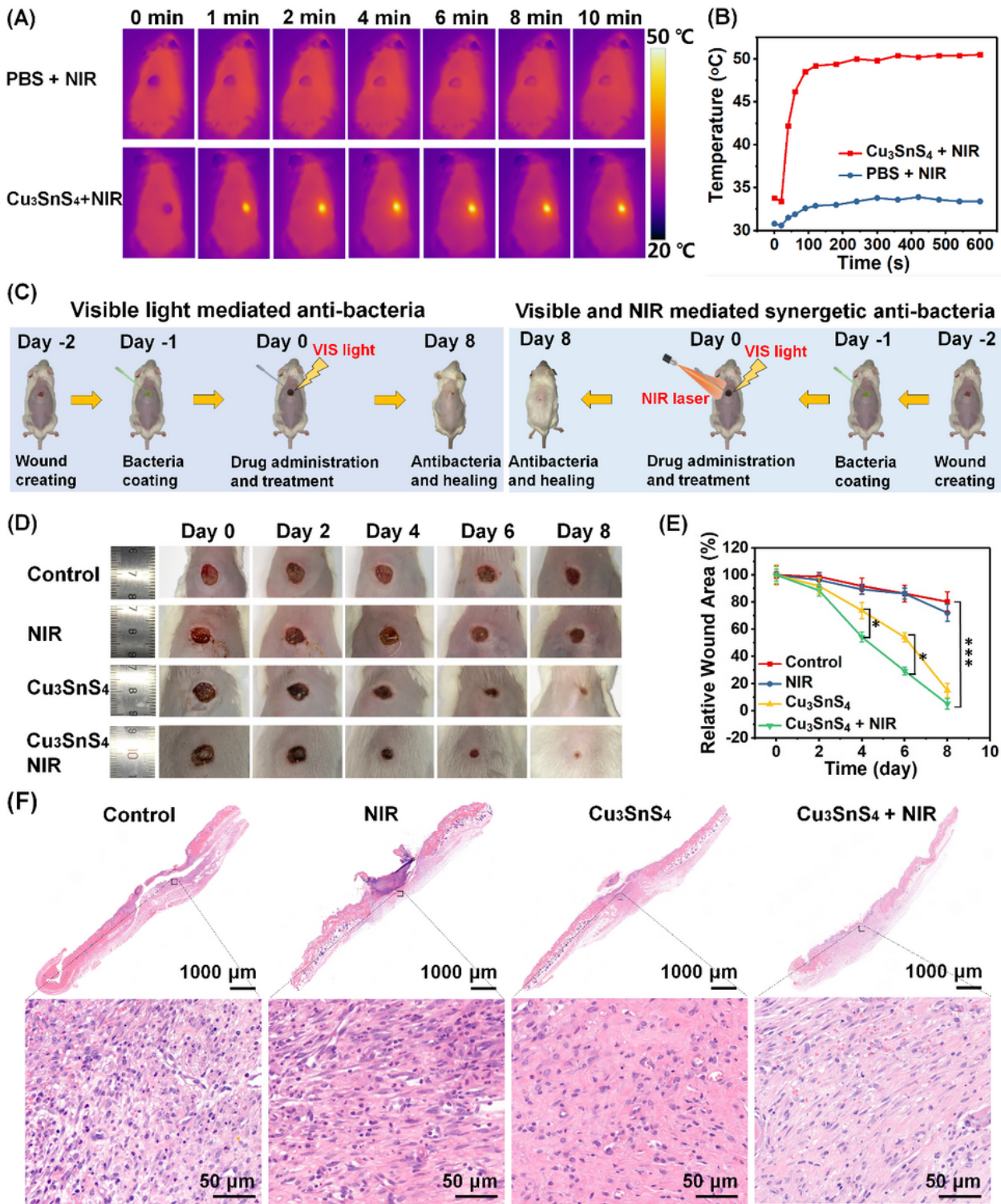


Figure 6

(A) *In vivo* thermal infrared images of mice after different treatments. Mice were treated with PBS or Cu₃SnS₄ NFs followed by NIR laser irradiation for different times. (B) Corresponding temperature change of wounds of mice after treatment with PBS or Cu₃SnS₄ NFs followed by 808 nm laser irradiation. (C) Scheme of the photo-activated antibacterial treatment processes. (D) Representative photographic images of ICR mice with MRSA-infected wounds after different treatments for 8 days: control (treated

with PBS), NIR (treated with PBS followed by NIR irradiation), Cu_3SnS_4 (treated with Cu_3SnS_4 NFs), and $\text{Cu}_3\text{SnS}_4 + \text{NIR}$ (treated with Cu_3SnS_4 NFs followed by NIR irradiation). (E) Corresponding changes of wound size in each group during the 8 days' treatments. Data are presented as means \pm SDs ($n = 6$). * $p < 0.05$, *** $p < 0.001$. (F) H&E staining of the dermal wound tissues on day 8 after different treatments. For NIR irradiation, 808 nm laser (1.0 W cm^{-2} , 10 min) were used.

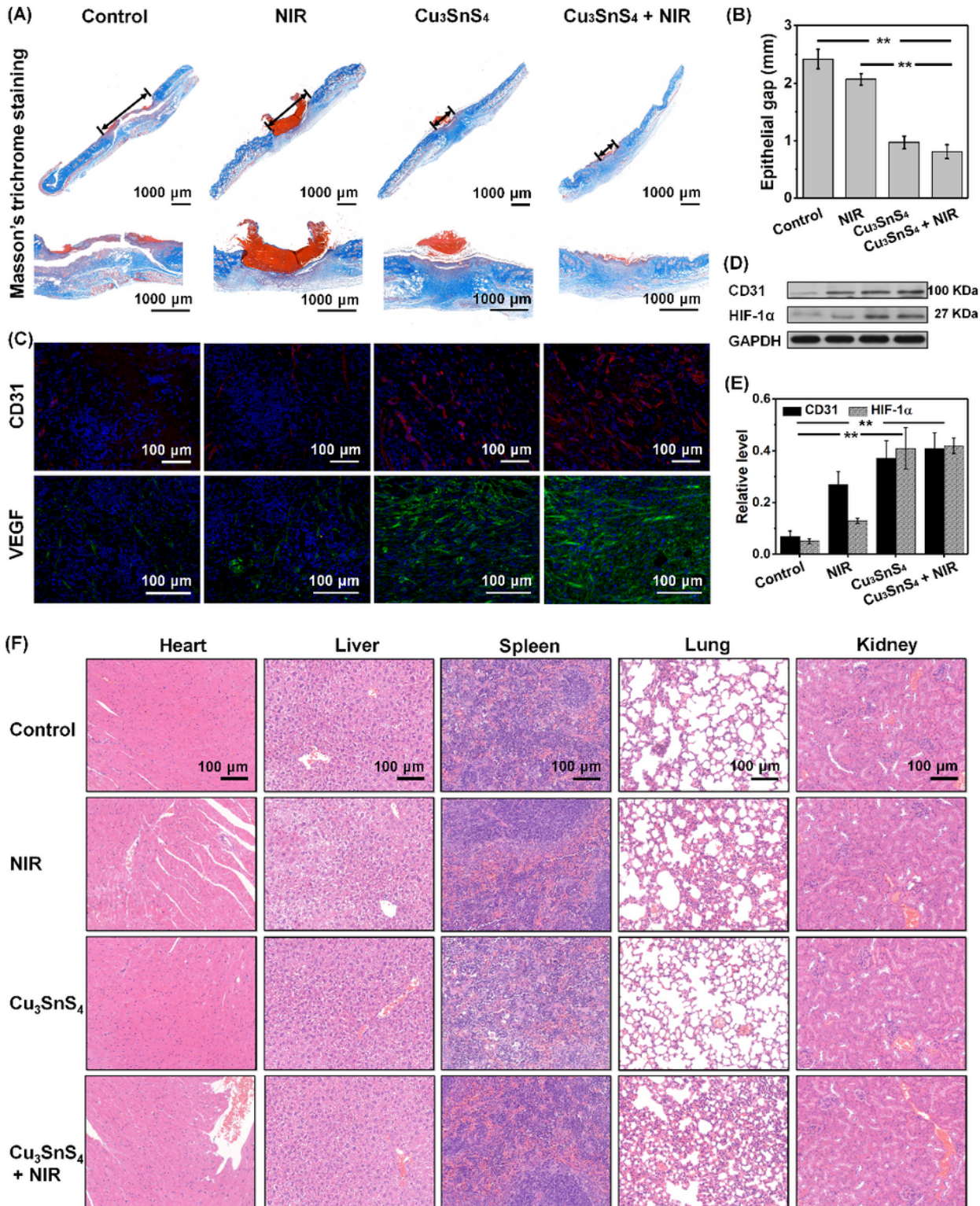
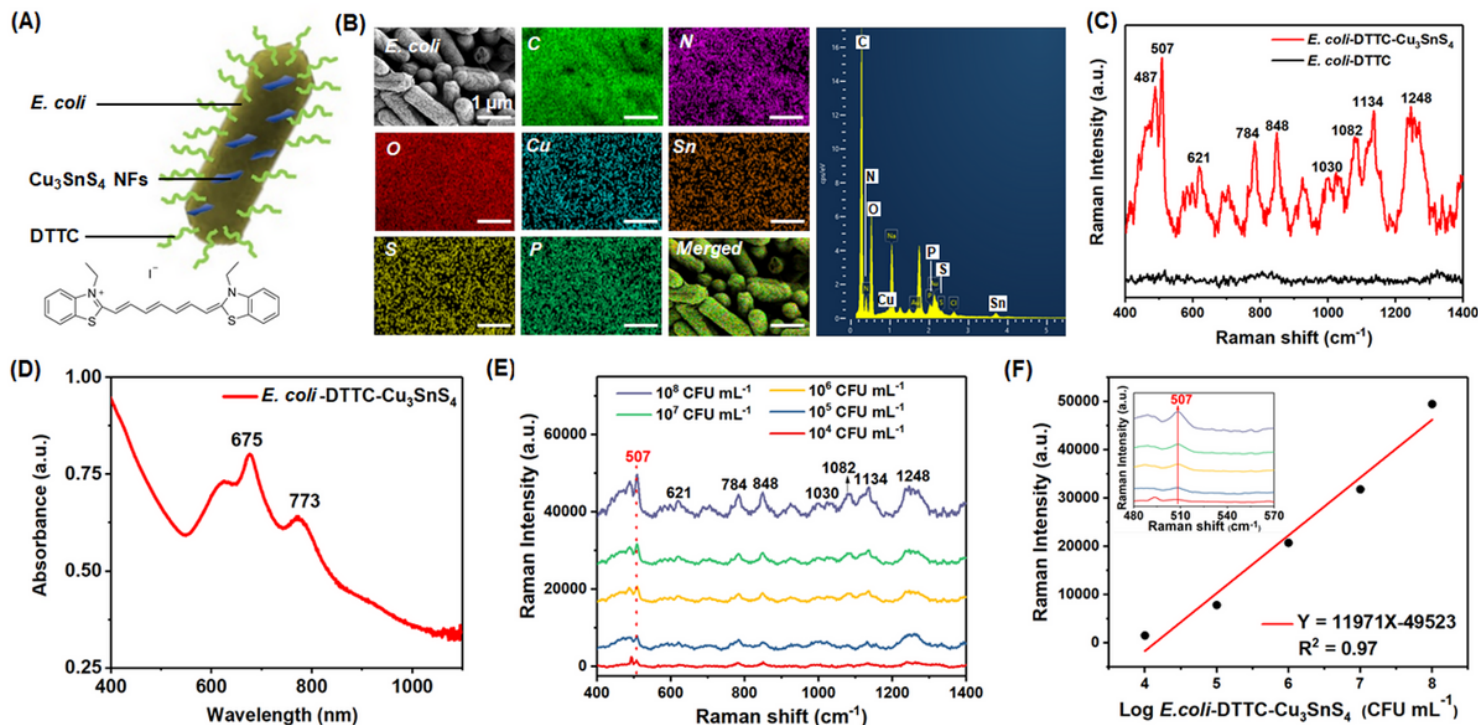


Figure 7

(A) Histopathological analysis of Masson's trichrome staining of wounds in mice on day 8 after different treatments. (B) Corresponding epithelial gap in each group after the treatment. (C) Representative histological images of CD31 and VEGF immunofluorescence staining of wound tissue in each group at the end of the 8 days' treatments. (D) Western blot analyses of CD31 and HIF-1 α expressions in wound of mice in each group at the end of 8 days' treatments. (E) Corresponding quantitative level of CD31 and HIF-1 α expressions in each group. (F) Representative H&E staining images of major organs after different treatments.

**Figure 8**

(A) Illustration of the *E. coli*-DTTC- Cu_3SnS_4 . (B) The SEM and EDS element mapping of the *E. coli*-DTTC- Cu_3SnS_4 . (C) The Raman spectra of *E. coli*-DTTC and *E. coli*-DTTC- Cu_3SnS_4 . (D) The UV/Vis/NIR absorption spectrum of the *E. coli*-DTTC- Cu_3SnS_4 . (E) *In vitro* SERS spectra of *E. coli*-DTTC- Cu_3SnS_4 under the excitation of a 785 nm laser. (F) Raman peak intensity versus $\text{Log } E. coli\text{-DTTC-}\text{Cu}_3\text{SnS}_4$ concentration at 507 cm^{-1} .

Supplementary Files

This is a list of supplementary files associated with this preprint. Click to download.

- [Graphicalabstract.png](#)
- [SupportingInformation.docx](#)